Solid State Ionics 286 (2016) 45–50

Contents lists available at ScienceDirect

Solid State Ionics

journal homepage: www.elsevier.com/locate/ssi

First principles investigation of the structural and electrochemical properties of $Na_4P_2S_6$ and $Li_4P_2S_6$

Larry E. Rush Jr., N.A.W. Holzwarth *

Department of Physics, Wake Forest University, Winston-Salem, NC 27109-7507, USA

ARTICLE INFO

Article history:
Received 13 November 2015
Accepted 8 December 2015
Available online xxxx

Keywords:
Na ion electrolyte
Solid electrolyte
Sodium and lithium thiophosphates
Na ion conductivity

ABSTRACT

First principles simulations are used to examine the structural and physical properties of $Na_4P_2S_6$ in comparison with its $Li_4P_2S_6$ analog. Four model structures are considered including the *C*2/*m* structure recently reported by Kuhn and co-workers from their analysis of single crystals of $Na_4P_2S_6$, and three structures related to the $P6_3/mcm$ structure with P site disorder found in 1982 by Mercier and co-workers from their analysis of single crystals of $Li_4P_2S_6$. The computational results indicate that both $Na_4P_2S_6$ and $Li_4P_2S_6$ have the same disordered ground state structures consistent with the $P6_3/mcm$ space group, while the optimized *C*2/*m* structures have higher energies by 0.1 eV and 0.4 eV per formula unit for $Na_4P_2S_6$ and $Li_4P_2S_6$, respectively. In modeling ionic conductivity in these materials, activation energies for Na ion vacancy migration were computed to be smaller than the Li analogs in all of the structural models. Interestingly, the results also indicate that if $Li_4P_2S_6$ could be prepared in the meta-stable *C*2/*m* structure, the Li ion vacancy migration would have very small barriers along certain channels. Simulations of $Na_4P_2S_6$ (*C*2/*m*)/Na interfaces indicate that they may be slightly less reactive than $Li_4P_2S_6$ ($P6_3/mcm$)/Li interfaces.

1. Introduction

In the development of solid state battery technology, there has been some recent progress in finding promising Na ion conducting materials [1]. Kuhn and co-workers [2] recently reported an interesting new structure for $Na_4P_2S_6$. Motivated by possibilities for Na ion electrolytes in advance of experimental measurements, we computationally examine the structural and physical properties of $Na_4P_2S_6$ in comparison with $Li_4P_2S_6$ [3], [4]. In particular, computations can be used to model the apparent structural differences between the two materials. $Li_4P_2S_6$ is known to have an interesting disordered structure which differs from Kuhn structure. Comparisons of the simulated Na and Li ion vacancy migration mechanisms for the various model structures can be used to predict ionic conductivity properties of the materials. Idealized interfaces between $Na_4P_2S_6$/Na are also investigated in order to predict electrolyte/anode interface stability.

This paper is organized as follows. Section 2 describes the computational methods used in this study. Section 3 presents the results for the energy and structural analysis in Section 3.1, for ion migration simulations in Section 3.2, and for interface simulations in Section 3.3. Discussions and conclusions are given in Section 4.

2. Methods

The calculational methods used in this work were the same as those used in previous studies of similar materials [5], [4]. Specifically, the calculations were based on density functional theory [6], [7], using the projector augmented wave (PAW) [8], [9] formalism. The PAW basis and projector functions were generated by the *ATOMPAW* [10] code and used in both the *ABINIT* [11] and *QUANTUM ESPRESSO* [12] packages. The exchange-correlation functional was the local density approximation (LDA) [13], which has been shown to give excellent results for similar materials provided that a systematic 2% underestimate of the lattice size is taken into account for each of the 3 dimensions [4]. The partial densities of states were calculated as described in previous work [5], [4], using weighting factors based on the charge within the augmentation spheres of each atom with radii $r_c^{Na} = 1.7$, $r_c^{Li} = 1.6$, $r_c^{P} = 1.7$, and $r_c^{S} = 1.7$ in bohr units.

The electronic structure calculations were performed with plane wave expansions of the wavefunctions including $|\mathbf{k}+\mathbf{G}|^2 \le 64\,\text{bohr}^{-2}$ and with a Brillouin zone sampling grid density of at least 0.003 bohr^{-3}/**k**-point. Structural parameters of the model systems, including the lattice constants and fractional atomic coordinates, were determined by optimizing the calculated total energy of each structure. The software program *FINDSYM* [14] was used to help analyze the symmetry properties of the optimized structures.

Vacancy, interstitial, and vacancy-interstitial pair defects were modeled using supercells consisting of 8 formula units. The simulations were performed on neutral supercells, adding a compensating uniform charge when modeling charged defects. The "nudged elastic band" (NEB) method [15], [16], [17], as included in the *QUANTUM ESPRESSO* package was used to estimate the Li^+/Na^+ migration energies, E_m, in supercell models. For this analysis it was assumed that 5 images between each meta-stable configuration were sufficient to estimate the path energies. The migration energies determined from the NEB

* Corresponding author.
E-mail address: natalie@wfu.edu (N.A.W. Holzwarth).

http://dx.doi.org/10.1016/j.ssi.2015.12.015
0167-2738/

calculations can be related to the experimental conductivity, σ, and to measurements as a function of temperature, T, through the Arrhenius relationship

$$\sigma = \frac{C}{T} e^{-E_A/kT}, \quad (1)$$

where C denotes a temperature independent constant for the sample, k denotes the Boltzmann constant, and E_A represents the activation energy for Na/Li ion migration. For nearly perfect crystals, thermal processes must initiate the formation of a vacancy and interstitial pair with energy E_f, so that the activation energy is related to the migration energy, E_m, according to $E_A = E_m + \frac{1}{2}E_f$. For crystals with a significant population of native defects, we expect $E_A = E_m$ [18].

Visualizations were constructed using the *XCrySDEN* [19,20], *VESTA* [21] and *CrystalMaker* [22] software packages.

3. Results

3.1. Structural properties

Mercier's structural analysis [3] for $Li_4P_2S_6$ named the space group $P6_3/mcm$ (# 193) in the International Table of Crystallography) [23] and designated the P sites with Wyckoff label 4*e* and site symmetry 3.*m* as having fractional occupancy 0.5. We have recently re-examined $Li_4P_2S_6$ experimentally and computationally finding that the disorder can be explained in terms of energetic degeneracy in the placement of the P_2S_6 building blocks within the structure [4]. The structure for $Na_4P_2S_6$ found by Kuhn and co-workers [2] appears to be entirely different from the Mercier structure; however, upon closer examination, we find that it is possible to find a geometric relationship between all of the structures. In fact, as discussed below, our calculations indicate that the Kuhn structure is not the lowest energy structure of $Na_4P_2S_6$.

The four structural forms for both $Na_4P_2S_6$ and $Li_4P_2S_6$ that comprise the current study are summarized in Table 1 in terms of their optimized lattice parameters. The unique fractional coordinates of $Na_4P_2S_6$ and $Li_4P_2S_6$ in the four crystal structures are listed in Table 2. The four structures are labeled according to their space groups — $C2/m$, corresponding to the Kuhn structure [2], and $P\bar{3}1m$, *Pnnm*, and *Pnma*, corresponding to the structures labeled Struc. (b), (c), and (d) studied in Ref. [4]. $P\bar{3}1m$ corresponds to a subgroup of the Mercier space group. The other two structures, which happen to have the space groups *Pnnm* and *Pnma*, are constructed from larger supercells and are examples of the disordered Mercier structure [3].

Table 1
Lattice parameters for the four model structures of $Na_4P_2S_6$ and $Li_4P_2S_6$. For each structure, the table lists the space group labels and ID numbers [23] as well as Z, the number of formula units per unit cell. The results are given for the calculated lattice parameters (a, b, c, β), in Å and degree units, respectively, for the optimized structures. Corresponding experimental lattice parameters are listed in parentheses when available — Ref. [2] given in the $C2/m$ section and Ref. [4] given in the *Pnnm* section.

	$Na_4P_2S_6$	$Li_4P_2S_6$
C2/m; No. 12; Z = 2		
a (Å)	6.57 (6.725)	6.04
b (Å)	10.95 (11.222)	10.37
c (Å)	7.36 (7.542)	6.78
β (deg)	106.6 (107.03)	106.2
P$\bar{3}$1m; No. 162; Z = 1		
a (Å)	6.34	5.95
c (Å)	6.97	6.37
Pnnm; No. 58 Z = 2		
a (Å)	7.09	6.41 (6.55)
b (Å)	6.31	5.95 (6.05)
c (Å)	10.90	10.28
Pnma; No. 62 Z = 4		
a (Å)	12.59	11.89
b (Å)	10.93	10.29
c (Å)	7.09	6.41

Table 2
Computed unique fractional coordinates for $Na_4P_2S_6$ and $Li_4P_2S_6$ in the four crystal structures. For comparison, fractional coordinates for $Na_4P_2S_6$ in the $C2/m$ structure reported by Ref. [2] is also given as indicated with "*". The site multiplicity and label is listed in the second column in terms of the Wyckoff notation [23].

Atom	Site	$Na_4P_2S_6$	$Li_4P_2S_6$
C2/m; No. 12			
Na/Li	4*g*	(0, 0.339,0) (0, .337, 0)*	(0, 0.333, 0)
Na/Li	4*h*	$(0, 0.186, \frac{1}{2})$ $(0, 0.185, \frac{1}{2})$*	$(0, 0.178, \frac{1}{2})$
P	4*i*	(0.054, 0, 0.160) (0.053, 0, 0.156)*	(0.056, 0, 0.169)
S	4*i*	(0.789, 0, 0.247) (0.794, 0, 0.241)*	(0.765, 0, 0.260)
S	8*j*	(0.726, 0.346, 0.232) (0.723, 0.350, 0.231)*	(0.738, 0.335, 0.240)
P$\bar{3}$1m; No. 162			
Na/Li	2*c*	$(\frac{1}{3}, \frac{2}{3}, 0)$	$(\frac{1}{3}, \frac{2}{3}, 0)$
Na/Li	2*d*	$(\frac{1}{3}, \frac{2}{3}, \frac{1}{2})$	$(\frac{1}{3}, \frac{2}{3}, \frac{1}{2})$
P	2*e*	(0, 0, 0.165)	(0, 0, 0.176)
S	6*k*	(0.308, 0, 0.240)	(0.331, 0, 0.248)
Pnnm; No. 58			
Na/Li	4*e*	(0, 0, 0.341)	(0, 0, 0.334)
Na/Li	4*f*	$(0, \frac{1}{2}, 0.824)$	$(0, \frac{1}{2}, 0.832)$
P	4*g*	(0.161, 0.000, 0)	(0.174, 0.000, 0)
S	8*h*	(0.235, 0.845, 0.155)	(0.245, 0.834, 0.166)
S	4*g*	(0.232, 0.310, 0)	(0.246, 0.331, 0)
Pnma; No. 62			
Na/Li	8*d*	(0.632, 0.589, 0.000)	(0.626, 0.584, 0.000)
Na/Li	8*d*	(0.119, 0.579, 0.000)	(0.125, 0.583, 0.000)
P	4*c*	$(0.625, \frac{1}{4}, 0.160)$	$(0.625, \frac{1}{4}, 0.176)$
P	4*c*	$(0.625, \frac{1}{4}, 0.839)$	$(0.625, \frac{1}{4}, 0.829)$
S	8*d*	(0.297, 0.595, 0.235)	(0.292, 0.584, 0.244)
S	8*d*	(0.452, −0.095, 0.769)	(0.458, −0.084, 0.755)
S	4*c*	$(0.471, \frac{1}{4}, 0.760)$	$(0.459, \frac{1}{4}, 0.755)$
S	4*c*	$(0.781, \frac{1}{4}, 0.230)$	$(0.791, \frac{1}{4}, 0.245)$

The results in Table 1 show that the ratio of the measured and computed lattice constants for $Na_4P_2S_6$ in the $C2/m$ structure follows the expected 1.02 scaling very well based on the experimental results of Ref. [2]. Similarly, the computed lattice constants for $Li_4P_2S_6$, as approximated by the *Pnnm* and *Pnma* structures, also follow the expected 1.02 scaling based on the low temperature measurements of Ref. [4]. The computed fractional coordinates of $Na_4P_2S_6$ in the $C2/m$ structure agree very well with the experimental results of Ref. [2].

The four structures considered in this study are geometrically related. The $P\bar{3}1m$ structure (labeled as Struc. (b) in Ref. [4]) is based on a hexagonal bravais lattice shown in Fig. 1. The lattice parameters $a = b$ and c for $Na_4P_2S_6$ and $Li_4P_2S_6$ in this structure are given in Table 1. As will be shown below, the Kuhn [2] $C2/m$ structure can be derived from a orthorhombic supercell of the $P\bar{3}1m$ structure. The *Pnnm* and *Pnma* structures (labeled as Struc. (c) and (d) in Ref. [4]) represent 2 of many possible realizations of the disordered $P6_3/mcm$ structure of $Li_4P_2S_6$ analyzed by Mercier [3] based on orthorhombic supercells of the basic hexagonal structure.

The $P\bar{3}1m$ structure shown in Fig. 1 has two inequivalent Na positions indicated by the two shades of blue in the diagram. In the view projected along the c-axis (Fig. 1a) the two Na sites are superposed, while the perpendicular view (Fig. 1b) shows that each *d* site Na is located in a plane between the P_2S_6 units, while each *c* site Na is located in a plane which also contains the P_2S_6 units.

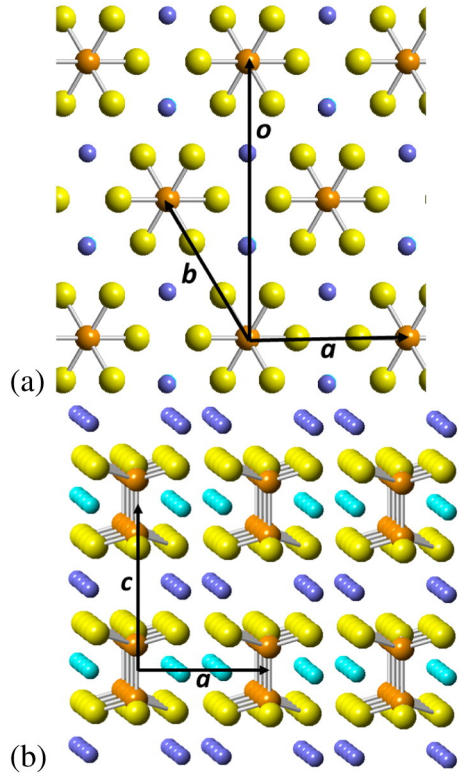

Fig. 1. Ball and stick model of $Na_4P_2S_6$ in the $P\bar{3}1m$ structure showing (a) a projection onto the hexagonal plane and (b) a view including the *c*-axis. The Na, P, and S sites are represented by blue, orange, and yellow balls, respectively. The two shades of blue indicate the inequivalent Na sites. The vectors **a**, **b**, and **c** represent the conventional hexagonal lattice vectors, while **o** shows a corresponding orthorhombic lattice vector. (For interpretation of the references to color in this figure legend, the reader is referred to the web version of this article.)

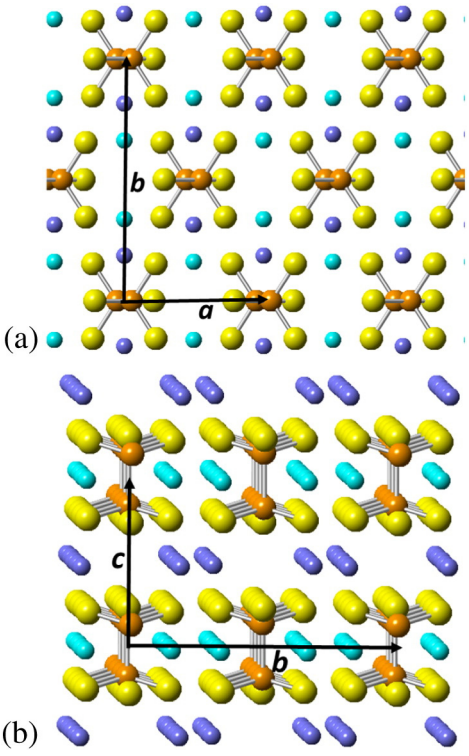

Fig. 2. Ball and stick model of $Na_4P_2S_6$ in the conventional $C2/m$ structure using the same ball convention as in Fig. 1.

The Kuhn structure [2] of $Na_4P_2S_6$ is shown in Fig. 2 in its conventional setting. Its relationship to the hexagonal vectors defined in Fig. 1 is as follows:

$$\mathbf{a}_{Kuhn} = \mathbf{a}_{hex}, \quad \mathbf{b}_{Kuhn} = \mathbf{o}_{hex}, \quad \mathbf{c}_{Kuhn} \rightarrow \mathbf{c}_{hex}. \tag{2}$$

While from the viewpoint of Fig. 2b, the structure looks very similar to Fig. 1, the $\mathbf{a}_{Kuhn}$ and $\mathbf{c}_{Kuhn}$ axes are no longer orthogonal. Fig. 2a shows the structure as projected in $\mathbf{a}_{Kuhn}$–$\mathbf{b}_{Kuhn}$ planes. Here it is evident that Na sites within a given $\mathbf{a}_{Kuhn}$–$\mathbf{b}_{Kuhn}$ plane are arranged in an approximately hexagonal pattern. The approximately hexagonal patterns of the sites with Wyckoff labels *g* and *h* are shifted with respect to each other in this projection unlike the superposed *c* and *d* Na sites found in the $P\bar{3}1m$ structure.

The other structures in this study, which happen to have the space group symmetries *Pnnm* and *Pnma*, were derived from analyzing the disorder structures of $Li_4P_2S_6$ in terms of the placements of the P_2S_6 units along the hexagonal *c*-axis. The *Pnnm* structure shown in Fig. 3 in its conventional setting, has the lattice relationships to the hexagonal vectors defined in Fig. 1 as follows:

$$\mathbf{a}_{\mathrm{pnnm}} = \mathbf{c}_{\mathrm{hex}}, \quad \mathbf{b}_{\mathrm{pnnm}} = \mathbf{a}_{\mathrm{hex}}, \quad \mathbf{c}_{\mathrm{pnnm}} = \mathbf{o}_{\mathrm{hex}}. \tag{3}$$

The *Pnma* structure shown in Fig. 4 in its conventional setting, has the lattice relationships to the hexagonal vectors defined in Fig. 1 as follows:

$$\mathbf{a}_{Pnma} = 2\mathbf{a}_{hex}, \quad \mathbf{b}_{Pnma} = \mathbf{o}_{hex}, \quad \mathbf{c}_{Pnma} = \mathbf{c}_{hex}. \tag{4}$$

In this case, the mappings are precise. As discussed in a previous work [4], these two structures represent two of many of the ground state configurations of $Li_4P_2S_6$ and presumably of $Na_4P_2S_6$.

Table 3 lists the computed heats of formation per formula unit for $Na_4P_2S_6$ and $Li_4P_2S_6$ in each of the structures, which is referenced to the standard states of the elements given in the CRC Handbook [24]. The results show the *Pnnm* and *Pnma* structures, which represent two possible realizations of the disordered $P6_3/mcm$ structure of $Li_4P_2S_6$ analyzed by Mercier [3], have the lowest energy for both $Na_4P_2S_6$ and $Li_4P_2S_6$. The $C2/m$ structure is 0.1 eV/formula unit higher in energy for $Na_4P_2S_6$ and by 0.4 eV/formula unit for $Li_4P_2S_6$. These results suggest that the synthesis method of Kuhn and co-workers [2] enabled them to produce this meta-stable phase of $Na_4P_2S_6$. The results also suggest that, because of its higher formation energy, it is unlikely that the analogous synthesis method would be successful for $Li_4P_2S_6$. The computational results also show that the $P\bar{3}1m$ structure is iso-energetic to the

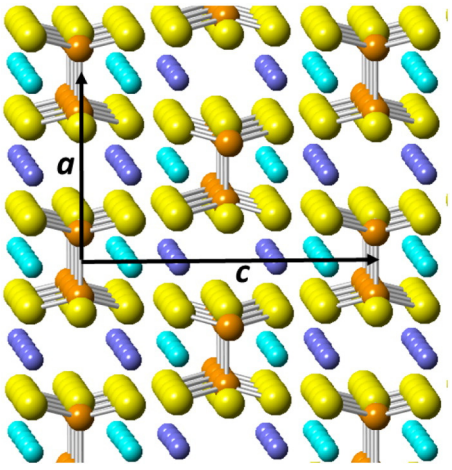

Fig. 3. Ball and stick model of $Na_4P_2S_6$ in the conventional *Pnnm* structure using the same ball convention as in Fig. 1.

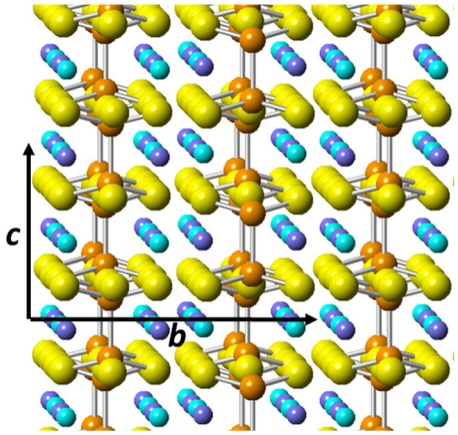

Fig. 4. Ball and stick model of $Na_4P_2S_6$ in the conventional *Pnma* structure using the same ball convention as in Fig. 1.

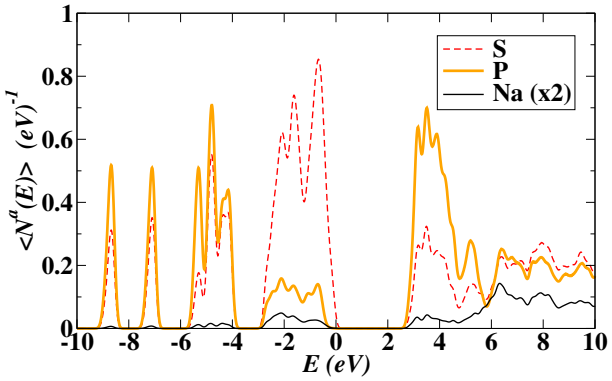

Fig. 5. Partial density of states plot for $Na_4P_2S_6$ in the *C*2/*m* structure. The contribution from Na has been scaled by a factor 2 in order to increase its visibility.

*C*2/*m* structure for $Na_4P_2S_6$ and is 0.03 eV/formula unit above the lowest energy structures for $Li_4P_2S_6$.

The partial densities of states for $Na_4P_2S_6$ are shown in Fig. 5 for the Kuhn structure; corresponding plots for the other three structures (not shown) are remarkably similar. The partial density of states for $Na_4P_2S_6$ is also very similar to that of $Li_4P_2S_6$ shown in Ref. [4], distinguished by the low energy phosphorus dimer states.

3.2. Ion migration

We considered Na/Li ion vacancy migration in three of the structures using supercells composed of 8 formula units. Table 4 lists the energies of each of the vacancy sites relative to the lowest energy site of each structure.

The $P\bar{3}1m$ structure results are given in Fig. 6. The path including sites with Wyckoff label *c* involves vacancy migration within planes perpendicular to the *c*-axis among the P_2S_6 units while the path including sites with Wyckoff label *d* involves vacancy migration within planes perpendicular to the *c*-axis between the P_2S_6 units. The latter path has a lower overall energy with a barrier height of 0.5 and 0.3 eV for Li and Na, respectively. The migration barrier for the vacancy migrating between *d* and *c* sites is $E_m = 0.7$ eV for both materials. Overall, the most favorable vacancy migration path for this material appears to be between *d* sites in each hexagonal plane between P_2S_6 units and the Na material has the lowest migration energy of $E_m = 0.3$ eV.

The Kuhn structure results are given in Fig. 7 where the similarities to the hexagonal structure results of Fig. 6 are evident where the sites with Wyckoff labels *g* and *h* for the *C*2/*m* structure map to the sites with Wyckoff labels *c* and *d* in the $P\bar{3}1m$ structure, respectively. Interestingly, however, the $h_1 \rightarrow h_2$ migration for the Li material in this structure has a very low energy barrier apparently due to a meta-stable interstitial site near the midpoint of the migration. These results indicate a very favorable Li ion vacancy migration path for this material if it can be made. For the Na material the Na ion vacancy migration barrier for this path is $E_m = 0.3$ eV. For this geometry, the most favorable path for Na ion vacancy migration consists of zigzag hops between *h* sites with net motion along the *a* axis. For this geometry, we also estimated the minimum energy to form a vacancy-interstitial pair of $E_f \approx 0.2$ eV, suggesting that the activation energy for Na ion diffusion should be $E_A \approx 0.4$ eV. In this case, the meta-stable interstitial sites are located at the centers of the distorted hexagonal pattern of the *h* site Na ions. More complicated migration mechanisms involving active participation of the interstitial sites might be worth further investigation.

The vacancy migration for $Na_4P_2S_6$ and $Li_4P_2S_6$ in the *Pnma* structure, representing the lowest energy paths for these materials, is shown in Fig. 8. For this structure each Na/Li has regions which are between P_2S_6 units and other regions which span P_2S_6 units and the migration energy barrier within a Na/Li plane is generally smaller than the barrier to migrate between planes. The migration energies within a plane is shown in Fig. 8. The maximum energy barrier within this path is $E_m =$ 0.6 and 0.4 eV for Li and Na, respectively. For this structure, vacancy migration in the *c*-direction is generally energetically more costly than migration within a hexagonal plane.

3.3. Surfaces and interfaces

In our previous study of interfaces of $Li_4P_2S_6$ with lithium metal, both experimentally and computationally, we found the interface to be unstable. Experimentally, symmetric cells of Li/$Li_4P_2S_6$/Li could be cycled only a few times. Computationally, optimized structures of Li/$Li_4P_2S_6$/Li supercells resulted in a number of broken P–S bonds and the formation Li_2S clusters at the interface [4]. Focusing on the Kuhn structure of $Na_4P_2S_6$, we computationally examined Na/$Na_4P_2S_6$/Na supercells. We found that it is possible to generate idealized perfect interfaces such as shown in Fig. 9. The structure is very sensitive to the initial configuration and structures with broken P–S bonds have lower energy, suggesting that the interface of $Na_4P_2S_6$ with sodium metal shown in Fig. 9 is marginally meta-stable, but perhaps slightly more stable than its Li analog. The partial density of states corresponding to the interface configuration of Fig. 9 is shown in Fig. 10. The Fermi level due to the metallic Na layers is aligned just below the unoccupied conduction bands of the electrolyte.

Table 3
Heats of formation (eV per formula unit) computed for the four optimized model structures labeled by their space groups and described in Tables 1 and 2.

$Na_4P_2S_6$	$Na_4P_2S_6$	$Li_4P_2S_6$
*C*2/*m*	−11.47	−12.07
$P\bar{3}1m$	−11.47	−12.42
Pnnm	−11.56	−12.46
Pnma	−11.56	−12.46

Table 4
Vacancy energies (in eV) for inequivalent sites as indicated by the Wyckoff site labels for three different crystal structures. In each case, the lowest energy site sets the zero of energy.

Space group	Site	$Na_4P_2S_6$	$Li_4P_2S_6$
*C*2/*m*; No. 12	Na/Li *g*	0.40	0.52
	Na/Li *h*	0.00	0.00
$P\bar{3}1m$; No. 162	Na/Li *c*	0.35	0.32
	Na/Li *d*	0.00	0.00
Pnma; No. 62	Na/Li *d*	0.15	0.11
	Na/Li *d*	0.00	0.00

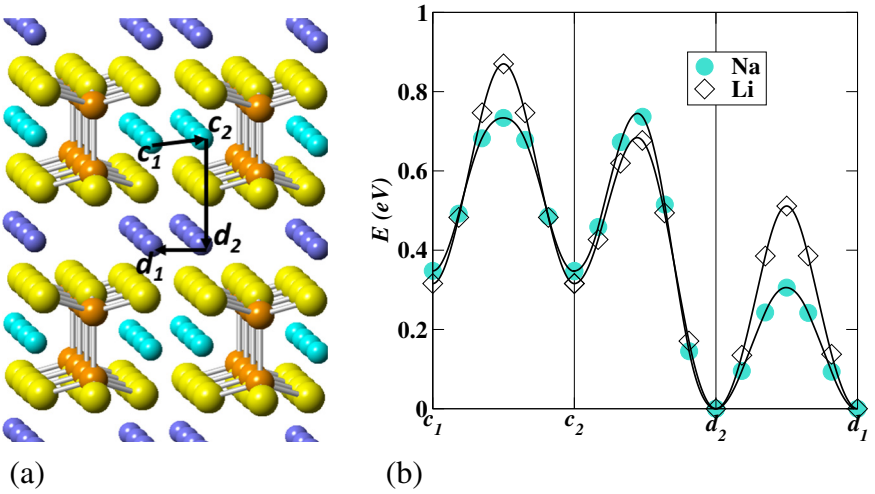

Fig. 6. (a) Structural diagram for vacancy migration in $P\bar{3}1m$ structure of $Na_4P_2S_6$ viewed with the perspective as Fig. 1b. The Li ion vacancy sites are labeled according to the Wyckoff notation. (b) NEB diagram for Na or Li ion vacancy migration in the $P\bar{3}1m$ structure of $Na_4P_2S_6$ and $Li_4P_2S_6$.

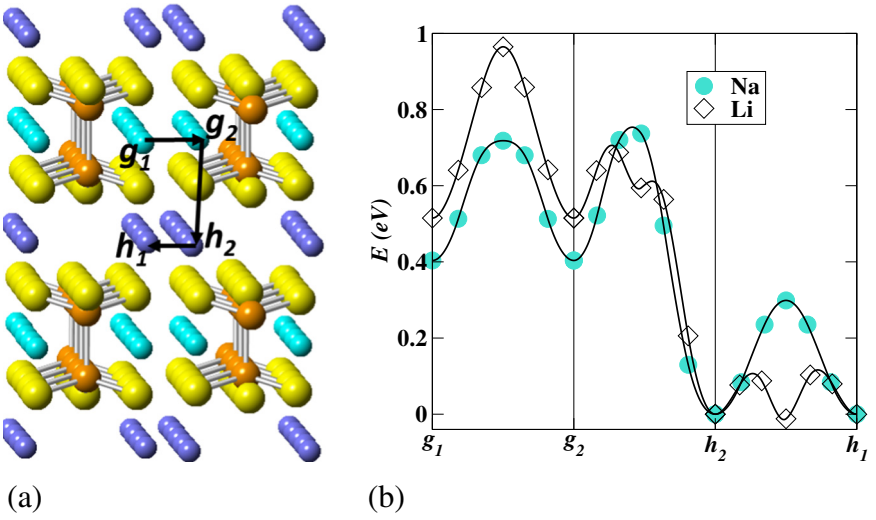

Fig. 7. (a) Structural diagram for vacancy migration in $C2/m$ structure of $Na_4P_2S_6$ viewed from the same perspective as Fig. 2b. The Li ion vacancy sites are labeled according to their Wyckoff notation. (b) NEB diagram for Na or Li ion vacancy migration in this structure of $Na_4P_2S_6$ and $Li_4P_2S_6$.

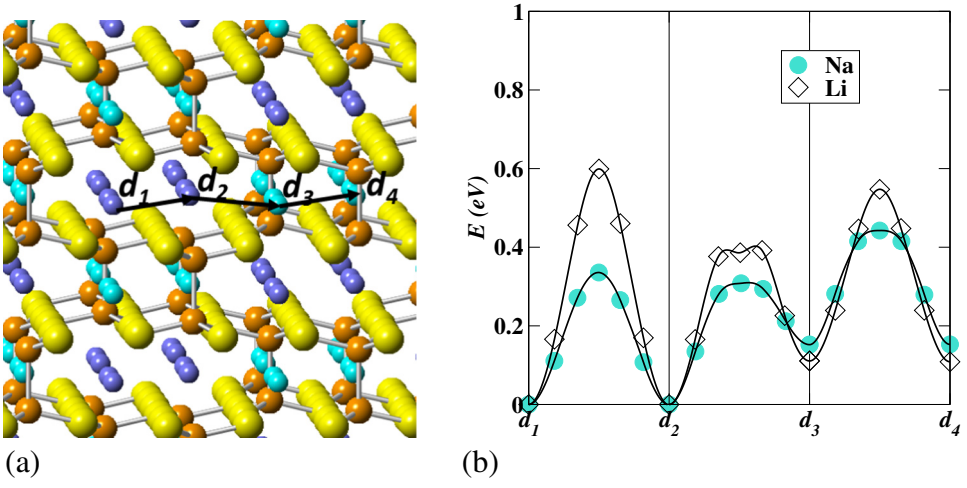

Fig. 8. (a) Structural diagram for vacancy migration in *Pnma* structure of $Na_4P_2S_6$ with the vertical direction representing the *c*-axis and the horizontal direction representing the *a*-axis. Li ion vacancy sites are labeled according to their Wyckoff notation. (b) NEB diagram for Na or Li ion vacancy migration in the *Pnma* structure of $Na_4P_2S_6$ and $Li_4P_2S_6$.

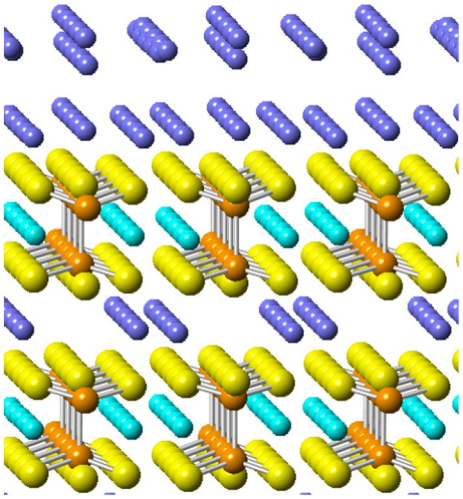

Fig. 9. Ball and stick model of optimized meta-stable configuration of $Na/Na_4P_2S_6/Na$ interface for the Kuhn structure cleaved parallel to the pseudo-hexagonal plane using the same ball convention as in Fig. 1.

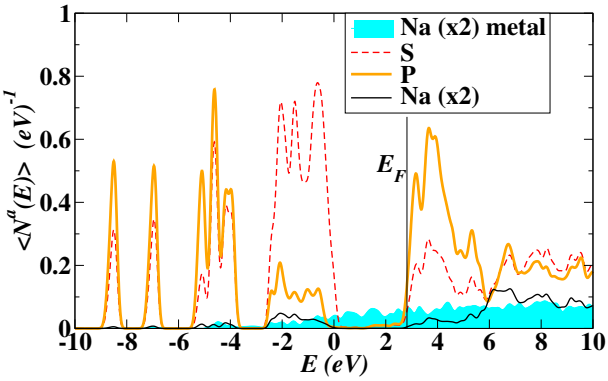

Fig. 10. Partial density of states diagram of interface system shown in Fig. 9. The metallic Na sites are indicated separately from the sites explicitly associated with the electrolyte. Both the metallic and ionic Na sites are scaled by a factor of 2 for visibility.

4. Discussions and conclusions

The results of the current simulation study of $Na_4P_2S_6$ and the growing importance of solid electrolytes with favorable Na ion conductivity encourage further experimental investigation of this material. The challenges for further experimental study include the determination of factors which control the formation of the Kuhn structure versus the Mercier structure which the simulations find to be more stable by 0.1 eV per formula unit. The simulations also suggest that the Kuhn structure, with its ordered placement of the P_2S_6 building blocks, may have favorable ionic conductivity as indicated by the estimated activation energy of $E_A = 0.4$ eV. To our knowledge, the conductivity of $Na_4P_2S_6$ has not yet been measured.

Acknowledgments

This work was supported by NSF grants DMR-1105485 and DMR-1507942. Computations were performed on the Wake Forest University DEAC cluster, a centrally managed resource with support provided in part by the University.

References

[1] A. Hayashi, K. Noi, M. Tanibata, N.a.d. Nagao, M. Tatsumisago, J. Power Sources 258 (2014) 420–423.
[2] A. Kuhn, R. Eger, J. Nuss, B.V. Lotsch, Z. Anorg. Allg. Chem. 640 (5) (2014) 689–692.
[3] R. Mercier, J.P. Malugani, B. Fahys, J. Douglade, G. Robert, J. Solid State Chem. 43 (1982) 151–162.
[4] Zachary D. Hood, Cameron Kates, Melanie Kirkham, Shiba Adhikari, Chengdu Liang, N.A.W. Holzwarth, Solid State Ionics 284 (2016) 61–70.
[5] N.D. Lepley, N.A.W. Holzwarth, A.D. Yaojun, Phys. Rev. B 88 (2013), 104103 (11 pp.).
[6] P. Hohenberg, W. Kohn, Phys. Rev. 136 (1964) B864–B871.
[7] W. Kohn, L.J. Sham, Phys. Rev. 140 (1965) A1133–A1138.
[8] P.E. Blöchl, Phys. Rev. B 50 (1994) 17953–17979.
[9] N.A.W. Holzwarth, G.E. Matthews, R.B. Dunning, A.R. Tackett, Y. Zeng, Phys. Rev. B 55 (1997) 2005–2017.
[10] N.A.W. Holzwarth, A.R. Tackett, G.E. Matthews, Comput. Phys. Commun. 135 (2001) 329–347 (Available from the website) http://pwpaw.wfu.edu.
[11] X. Gonze, B. Amadon, P.M. Anglade, J.M. Beuken, F. Bottin, P. Boulanger, F. Bruneval, D. Caliste, R. Caracas, M. Cote, T. Deutsch, L. Genovese, P. Ghosez, M. Giantomassi, S. Goedecker, D.R. Hamann, P. Hermet, F. Jollet, G. Jomard, S. Leroux, M. Mancini, S. Mazevet, M.J.T. Oliveira, G. Onida, Y. Pouillon, T. Rangel, G.M. Rignanese, D. Sangalli, R. Shaltaf, M. Torrent, M.J. Verstraete, G. Zerah, J.W. Zwanziger, Comput. Phys. Commun. 180 (12) (2009) 2582–2615 (Code is available at the website) http://www.abinit.org.
[12] P. Giannozzi, S. Baroni, N. Bonini, M. Calandra, R. Car, C. Cavazzoni, D. Ceresoli, G.L. Chiarotti, M. Cococcioni, I. Dabo, A.D. Corso, S. de Gironcoli, S. Fabris, G. Fratesi, R. Gebauer, U. Gerstmann, C. Gougoussis, A. Kokalj, M. Lazzeri, L. Martin-Samos, N. Marzari, F. Mauri, R. Mazzarello, S. Paolini, A. Pasquarello, L. Paulatto, C. Sbraccia, S. Scandolo, G. Sclauzero, A.P. Seitsonen, A. Smogunov, P. Umari, R.M. Wentzcovitch, J. Phys. Condens. Matter 21 (39) (2009), 394402 (19pp. Available from the website) http://www.quantum-espresso.org.
[13] J.P. Perdew, Y. Wang, Phys. Rev. B 45 (1992) 13244–13249.
[14] H.T. Stokes, D.M. Hatch, J. Appl. Crystallogr. 38 (2008) 237–238 (Available from the webpage) http://iso.byu.edu/iso/isotropy.php.
[15] H. Jónsson, G. Mills, K.W. Jacobsen, in: B.J. Berne, G. Ciccotti, D.F. Coker (Eds.), Classical and Quantum Dynamics in Condensed Phase Simulations, World Scientific, Singapore 1998, pp. 385–404.
[16] G. Henkelman, B.P. Uberuaga, H. Jónsson, J. Chem. Phys. 113 (2000) 9901–9904.
[17] G. Henkelman, H. Jónsson, J. Chem. Phys. 113 (2000) 9978–9985.
[18] R. Anthony, Basic Solid State Chemistry, second ed.John Wiley & Sons, LTD, 1999.
[19] A. Kokalj, J. Mol. Graph. Model. 17 (1999) 176–179 (Code available at the website) http://www.xcrysden.org.
[20] A. Kokalj, Comput. Mater. Sci. 28 (2003) 155–168.
[21] K. Momma, F. Izumi, Appl. Crystallogr. 44 (2011) 1272–1276 (Code available from the website) http://jp-minerals.org/vesta/en/.
[22] Crystalmaker, 2015. Proprietary software available from the website www.crystalmaker.com.
[23] T. Hahn (Ed.), International Tables for Crystallography, Volume A: Space-Group Symmetry, Fifth revised ed.Kluwer, 2002 (ISBN 0-7923-6590-9).
[24] W.M. Haynes (Ed.), CRC Handbook of Chemistry and Physics, 92ndth ed.CRC Press, Taylor & Francis Group, 2011 (ISBN 978-1-4398-5511-9).